Particle Image Velocimetry of a Highly Separated Transitional Shock-Wave/Boundary-Layer Interaction

Philipp L. Nel, Anne-Marie Schreyer
RWTH Aachen University, Templergraben 55, 52062 Aachen, Germany

Ferry F. J. Schrijer, Bas W. van Oudheusden
Faculty of Aerospace Engineering, Delft University of Technology, Kluyverweg 1, 2629 HS Delft, the Netherlands

This is an abstract for the 25th International Shock Interaction Symposium to be held in Delft, the Netherlands between 1 and 4 July 2024.

I. Introduction

Reynolds numbers at altitude on transonic fans can result in a laminar boundary layer persisting on the suction side of a transonic fan blade up to the shock-wave/boundary-layer interaction (SBLI). With the increasing loading of transonic fan blades, there is a growing interest in studying strong transitional SBLIs [1]. In a transitional SBLI with sufficiently large shock-induced separation, a shock oscillation mechanism occurs, characterized by the growth and natural suppression of the upstream laminar part of the separation bubble [1], [2]. This interaction is studied experimentally at Mach 2.3 in the High Speed Aerodynamics Laboratory at Delft University of Technology using particle image velocimetry (PIV). In a previous study by the authors [3], high-speed Schlieren imaging at 100,000 fps and spark light shadowgraphy was used to study the transition and oscillation mechanics. A characteristic length scale, based on the distance the periodically upstream propagating (laminar) separation shock travel was proposed. The study validated LES simulations with experimental results, showing matching Strouhal frequencies. Spark light shadowgraphs confirmed the shifting transition location observed in LES. Numerical simulations indicated a strong dependency on free stream turbulence levels. Dominant oscillation frequencies shifted significantly for turbulent SBLIs. Dynamic Mode Decomposition showed distinct mode shapes for laminar and turbulent interactions, with the laminar SBLI oscillation mode strongly linked to the separation bubble. The PIV aims to support these studies by quantitative measurements at mid span.

II. Particle Image Velocimetry

Different parts of the PIV light sheet at mid span are captured using a LaVision Imager LX (1624×1236, 130 pix/mm) with 105mm Nikon Nikkor lens. The flow was seeded with TiO_2 particles (30 nm crystal size, response time $\tau_p = 2.48$ µs), which are illuminated with a double-pulse YAG Spectra Physics Quanta Ray PIV-laser (140 mJ per pulse). The laser beam can be seen guided into the probe which delivers the light sheet to the test section. Figure 1 shows some photographs of the PIV experiment.

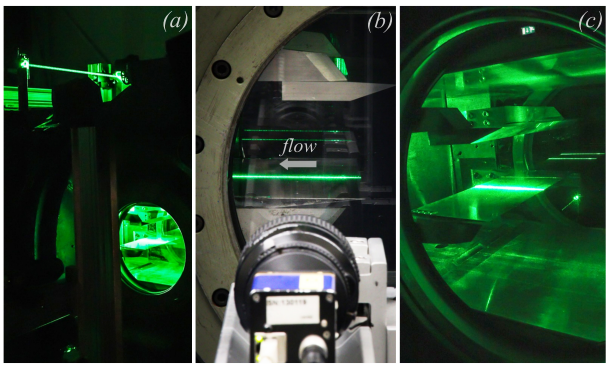

Fig. 1 PIV setup: (a) Laser beam guided into the probe, delivering the light sheet to the test section (flow right to left). (b) Camera directed at the test section. (c) Close-up of the test section with the light sheet at mid-span, showing laser light source in the background.

As for the field of view, one case shows the interaction region and the impinging and leading edge shock waves (FOV 62mm, 26.2 pix/mm, 1100 snapshots), the other two cases are zoomed in to the interaction region (FOV 35.5mm, 45.75 pix/mm), showing the bulk of the separation bubble (1050 snapshots) and an upstream position in order to show compression waves from the flat laminar part of the separation bubble (400 snapshots). Vector processing is performed using LaVision DaVis with the multi-pass (64×64→16×16) approach, utilizing adaptive PIV weighting to better capture gradients.

In the supersonic experiments, sporadic large areas with low seeding density necessitate post-processing to identify and eliminate these areas, characterized by logically unnatural gradients and unresolved clusters. This step ensures a cleaner input, resulting in more accurate standard deviations and modes from Proper Orthogonal Decomposition (POD). A comparison of POD modes from

the raw vs. post processed y-velocity data can be seen in Figure 3 for an upstream location in the SBLI. It can be seen that the modes in the bottom row have a cleaner decomposition and therefore allow more insights into the physics than the top row.

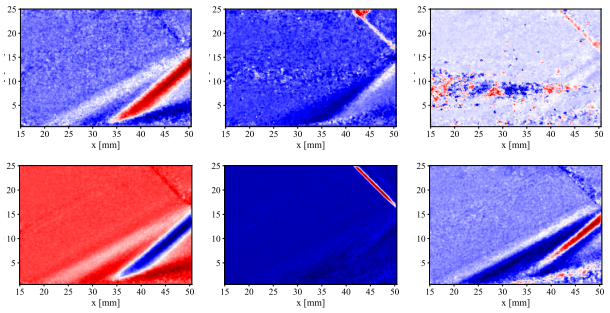

Fig. 2 Comparison of first POD modes from unprocessed data (top), and for post-processed data (bottom)

Additionally, post-processing avoids the need for larger interrogation windows during vector processing, which is crucial for gaining accurate insights into the instantaneous flow field. The used methods such as automatic phase detection and averaging with a Pearson correlation matrix benefit from this cleaner data, as they discard low-ranked phases likely to contain outliers, leading to more reliable phase averages. Consequently, in order to achieve these objectives, the raw results are processed with a Python code which is described in the next section.

A. Post-Processing Algorithm

1. Summary

The process begins with automatically computing phase-averaged images to maximize the differences between calculated averaged phases. Since this step uses the raw data, identified phases that correlate due to naturally under-resolved areas (if any) can be excluded by user judgement, which the algorithm then will avoid in the outlier-replacement step.

For outlier removal, the Pearson correlation coefficient is calculated between each image and automatically determined phase-averaged reference images. This correlation matrix helps in identifying and sorting images based on their average correlations. Reference images maximize the difference between their average correlations, ensuring distinct phases that capture the variability among the images effectively.

Outliers in the calculated velocity arrays (let us refer to these arrays as images) are marked based on two criteria: threshold-based and jump-based outliers. Threshold-based outliers are identified if a pixel's value falls outside a specified range, while jump-based outliers are marked if there's a significant value jump between a pixel and its neighbours. For each identified outlier cluster, weighted replacement is performed using a reference image, where the weight matrix ensures a smooth blend of values from the reference image into the current image.

The cleaned images are then used in the automatic phase detection algorithm to calculate the final most relevant phases. By forcing a higher number of phases than expected, the method automatically separates low-ranked phases likely containing unfixed outliers, thereby removing bad images from phase averaging. This comprehensive post-processing algorithm preserves the statistical integrity of the velocity field without relying on interpolation or large interrogation windows in vector processing.

2. Procedure

The first step for outlier removal is to automatically compute phase-averaged images such that the difference between the calculated averaged phases is maximised. This is done after a median filter. Phases which are automatically identified and correlate due to naturally under-resolved areas (for example, just upstream of the shock-shock interaction of the impinging and reflected shock), are excluded later on in an outlier-replacement step of the algorithm.

If Q is a 3D array of shape (N, H, W) where N is the number of images, and H and W are the height and width of each image, respectively, each image is flattened into a vector of size HW. These vectors q exist as $q_i \in \mathbb{R}^{HW}$ for $i = 1, 2, \ldots, N$. The correlation between two images q_i and q_j is given by their Pearson correlation coefficient:

$$\mathrm{r}(q_i, q_j) = \frac{\sum_k (q_i[k] - \bar{q}_i)(q_j[k] - \bar{q}_j)}{\sqrt{\sum_k (q_i[k] - \bar{q}_i)^2}\sqrt{\sum_k (q_j[k] - \bar{q}_j)^2}}$$

where $\bar{q}_i$ and $\bar{q}_j$ are the mean values of q_i and q_j, respectively. The process begins with the calculation of the correlation matrix C of size $N \times N$, where each entry C_{ij} represents the correlation between images q_i and q_j: $C_{ij} = \mathrm{r}(q_i, q_j)$. Next, the average correlation for each image is computed as $\mathrm{r}_i^{\mathrm{avg}} = \frac{1}{N}\sum_{j=1}^{N} C_{ij}$, and the images are then sorted based on their average correlations.

Images are sorted as indices of the average correlation of each image with all other images $\mathrm{r}^{\mathrm{avg}}$. This sorting process assigns each image a specific rank (index). Next, select the n images (number of desired phases) where the differences $|\mathrm{r}^{\mathrm{avg}}_{\mathrm{indices}[k+1]} - \mathrm{r}^{\mathrm{avg}}_{\mathrm{indices}[k]}|$ are maximised (k refers to the sorted list index). Following this, n reference images R are selected such that the difference between their average correlations is maximised. This ensures that the selected phases are as distinct as possible, capturing the variability among the images. In other words, the largest gaps in the sorted indices are selected.

Subsequently, the correlation of each image with each

reference image is computed as $C_{i,j} = r(q_i, R_j)$, where j is the phase number. Each image q_i is then assigned to the phase of the reference image with which it has the highest correlation, i.e., $\text{Phase}(q_i) = \arg\max_j C_{i,j}$.

Finally, for each phase, the averaged image is then computed over the set of images assigned to the phase.

Now that the relevant phases are identified, the Pearson coefficient is then computed between every image I and each of the automatically calculated, optimized phase-averaged reference images R of number n:

$$r = \frac{\sum_{i=1}^{n}(I_i - \bar{I})(R_i - \bar{R})}{\sqrt{\sum_{i=1}^{n}(I_i - \bar{I})^2}\sqrt{\sum_{i=1}^{n}(R_i - \bar{R})^2}}$$

The phase-averaged image with the highest Pearson correlation coefficient is selected as the reference image for outlier replacement of a specific image, ensuring that the replacement values come from a contextually relevant flow field.

Outliers in the original image (without median filtering to better identify non-physical areas) are marked based on two criteria:

1. Threshold-Based Outliers: A pixel $I_{i,j}$ is marked as a threshold-based outlier outlier O_t if:

$$I_{i,j} < q_{\min} \quad \text{or} \quad I_{i,j} > q_{\max}$$

Where q is the flow quantity.

2. Jump-based Outliers: A pixel $I_{i,j}$ is marked as an outlier if there is a significant jump between its value and any of its four direct neighbours (top, bottom, left, right), and neither the pixel itself nor its neighbours have a value of zero. Furthermore, the jump is significant if it exceeds a threshold T_{jump} of 10% of $q_{\max} - q_{\min}$:

$$O_{\text{jump}}(i,j) = \begin{cases} 1 & \text{if } I_{i,j} \neq 0 \\ & \text{and } 0 \notin N_{i,j} \\ & \text{and } \exists I_{k,l} \in N_{i,j} \\ & \text{such that } |I_{i,j} - I_{k,l}| > T_{\text{jump}} \\ 0 & \text{otherwise} \end{cases} \quad (1)$$

where neighbours $N_{i,j} = \{I_{i-1,j}, I_{i+1,j}, I_{i,j-1}, I_{i,j+1}\}$

For each labeled outlier cluster (this excludes single pixel outliers with no other outliers at a radius of 3 pixels), weighted replacement is performed using the reference image R. The weight matrix W is of size $(2r+1) \times (2r+1)$, where r is the radius of the replacement window, defined by exponential decay:

$$W_{dy,dx} = \exp\left(-\frac{S \cdot \sqrt{dy^2 + dx^2}}{r}\right)$$

where S is the transition strength. For each pixel (i, j) in a labeled outlier cluster, the replacement value is computed as:

$$I_{i+dy,j+dx} = (1 - W_{dy+r,dx+r}) \cdot I_{i+dy,j+dx} + W_{dy+r,dx+r} \cdot R_{i+dy,j+dx}$$

where (dy, dx) ranges over the window centered at (i, j).

This ensures that outlier pixels are replaced with contextually relevant values from the best-matching phase.

This transition function smoothly replaces outliers by blending values from the reference image with the original image using a weighted average. The weights are determined based on the distance from the outlier pixel, ensuring that closer pixels have a higher influence. Finally a weak median filter (radius of 2 pixels) is applied.

For the y velocity (v), it is found that the best result is obtained by combining the outliers detected (O_v) and those detected in the velocity magnitude (O_V), because of the approximate zero mean of v. For boolean matrices of identified outliers (Eq. 1), these two matrices may be conveniently combined with the logical OR operation ($O_{ij} = O_{vij} \vee O_{Vij}$).

Finally, the cleaned up images are used in the same automatic phase detection algorithm in order to calculate the final most relevant phases. In forcing a higher number of phases as the input than the expected number of phases (e.g. 5 vs 3), the combined method automatically separates the low-ranked phases which will likely contain images with outlier areas which could not be fixed in the outlier removal process, effectively removing bad images from phase averaging automatically.

This process preserves the relevant statistical integrity of the velocity field without using interpolation or large interrogation windows in vector processing.

III. Analysis of Results

It is already clear in the standard deviation of velocity magnitude, that there is dynamic behaviour of the separation bubble, reflected shock as well as a variation in the slip lines from the Mach stem. In order to analyse these effects more closely, we use Proper Orthogonal Decomposition. The advantage of the PIV results are that we can get a better understanding of the grown and suppressed separation bubble at mid span, which dominates the oscillation.

The POD modes in Figure 3 are marked with the order of their eigenvalue significance (Figure 4). The most dominant mode (1) shows the dominant size variation of the separation bubble due to suppression from upstream instabilities from the periodically forming and self-suppressing laminar separation upstream of the turbulent part of the separation bubble. The 2$^{\text{nd}}$ POD mode reflects the up and downstream movement-component of the separation bubble growth and suppression. Indeed the large scale

movement of the reflected shock wave, as expected, can be seen in the 3rd POD mode. The rest of the shown POD modes are largely related to large-scale vortex shedding in the shear layer of the separation bubble.

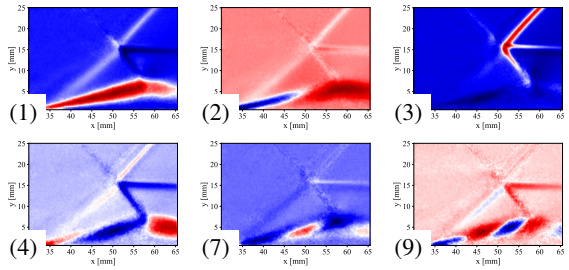

Fig. 3 POD modes showing dominant spatial coherent separation bubble and reflected shock behaviour

The closed nature of the separation bubble can be seen in the time averaged flow field with streamlines in Figure 5.

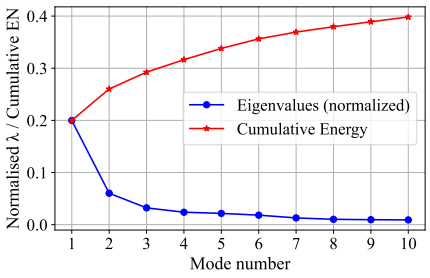

Fig. 4 Eigenvalue significance.

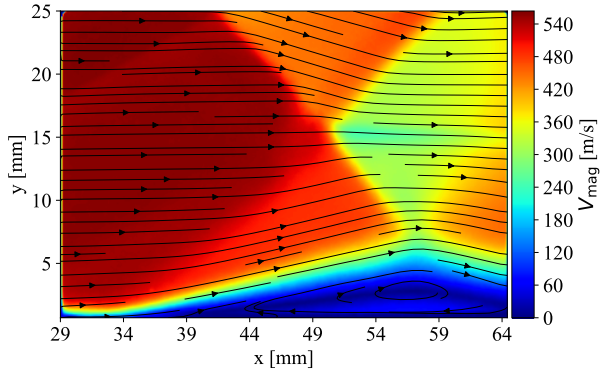

Fig. 5 Downstream: averaged velocity magnitude with streamlines.

The wall-normal Reynolds stress, given by

$$\overline{v'v'} = \frac{1}{N}\sum_{i=1}^{N}(v_i')^2,$$

and normalized by the square of the free stream velocity (Figure 7), provides insights into the vertical mixing and shows that the sudden turbulent thickening which is linked to a turbulent separation shock. Furthermore, note the abrupt increase in vertical mixing after the impingement location (x = 60mm).

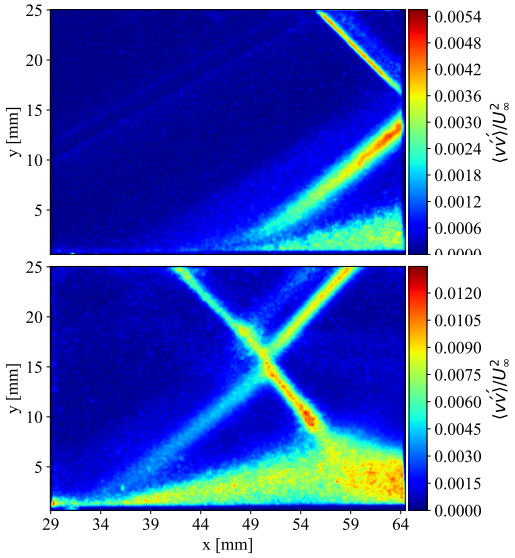

Fig. 7 Wall-normal Reynolds stress $\overline{v'v'}$ (downstream).

A. Upstream Laminar Separtion

The upstream laminar section of the separation bubble plays a crucial role in the mechanics of shock oscillation. This section grows upstream at the speed of acoustic wave propagation and periodically vanishes due to turbulence from Kelvin-Helmholtz instabilities on the shear layer. These instabilities are pulled far upstream, eventually reaching a distance significant enough to wash away the laminar part of the separation. This occurs because the turbulence cuts off the subsonic channel into which the laminar section had grown. This channel (laminar part of the separation) is extremely thin, and can only be seen through the presence of faint upstream compression waves which we shall refer to as laminar separation shocks. Furthermore, the distance by which the laminar separation bubble grows is crucial for the shock oscillation frequency, as it is the characteristic length scale for the Strouhal number. This section therefore focuses on the upstream view and attempts to highlight this part of the flow physics.

Inspection of Figure 8 reveals the laminar separation shock emanating from between x = 20mm for (a) and x = 15mm for (b). In (c) and (d), the thin laminar separation as well as a part of the turbulent separation is washed away, and therefore we only see a turbulent separation shock. The upstream compression waves can be seen in the POD modes of wall normal velocity (Figure 9). The first and second (not shown) modes are a decomposition of the turbulent separation shock. The 3rd (not shown) mode shows a slight variation of the incoming shock (or noise due to the PIV capturing of the strong incoming shock, which optically distorts the particles). The 4$^{\text{th}}$ mode shows the compression caused by the laminar part of the separation shock due to the slight thickening (this is a periodic occurrence [1]–[3]). For the minimum and maximum positions of the laminar separation shock, the first POD mode where this becomes clear is selected (5), which should therefore be based on the most common scenario. The laminar separation shock commonly appears between (b) and (c) on the figure. The difference in abscissae at the x point of emanation equates to the characteristic length scale which dominates the frequency of the entire dominant shock oscillation mechanism (as of now unpublished). It can be seen to be in the order of 11-12mm. Note that the range of laminar separation shock is situated slightly downstream from where it was seen in Spark Light shadowgraphs and high speed Schlieren [3]. This is because at mid span, there is a symmetrical region where the shock curves downstream, which was seen on the oil flow visualisation [3].

The influence of the laminar part of the separation on the averaged flow field can also be seen in Figure 10 in that, when following the streamline from the bottom left, there is a slight curvature upstream of the abrupt thickening caused by the transition.

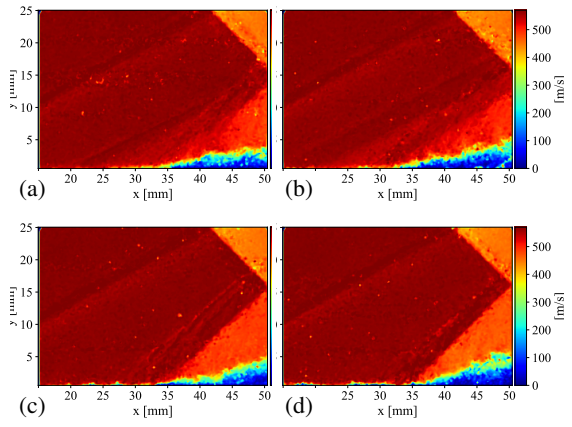

Fig. 8 Upstream velocity magnitude. (a) (b): upstream grown phase, a laminar separation shock is visible upstream. (c) (d): downstream phase, no laminar separation shock.

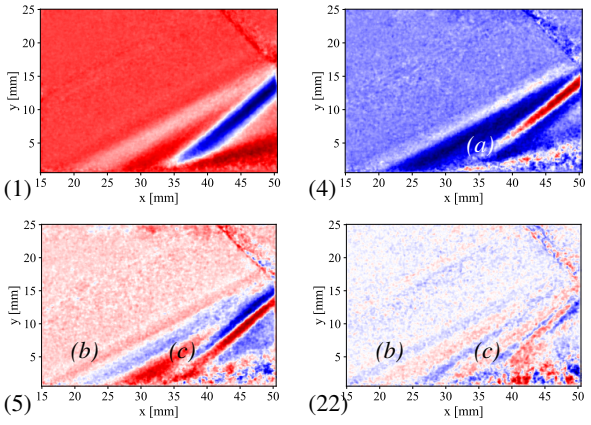

Fig. 9 POD modes of wall normal velocity showing upstream waves. Eigenvalue order of significance marked.

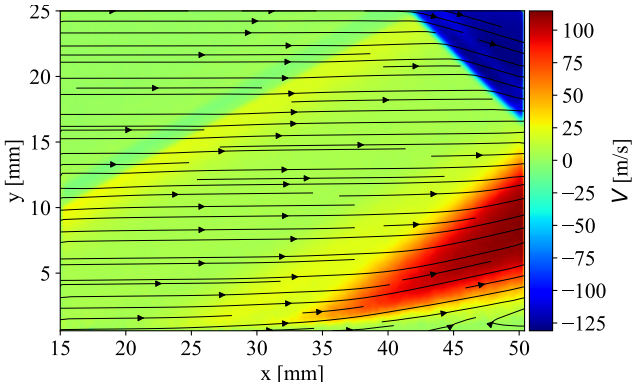

Fig. 10 Upstream: averaged contours of v velocity accompanied by streamlines.

References

[1] P. L. Nel, A.-M. Schreyer, C. Janke, *et al.*, "Effect of transition on self-sustained shock oscillations in highly loaded transonic rotors," *AIAA Journal*, vol. 62, no. 6, pp. 2063–2075, 2024. DOI: 10.2514/1.J063378. eprint: https://doi.org/10.2514/1.J063378. [Online]. Available: https://doi.org/10.2514/1.J063378.

[2] P. L. Nel, A.-M. Schreyer, F. Schrijer, B. van Oudheusden, C. Janke, and M. Swoboda, "Research configuration to study shock oscillation mechanism in highly loaded transonic fans," *AIAA Journal*, unpublished.

[3] P. L. Nel, A.-M. Schreyer, F. Schrijer, *et al.*, "Shock oscillation mechanism of highly separated transitional shock-wave/boundary-layer interactions," *AIAA Journal*, unpublished.